The electronic landscape of the P-cluster of nitrogenase

Zhendong Li[1*], Sheng Guo[1], Qiming Sun[1], Garnet Kin-Lic Chan[1*]
Division of Chemistry and Chemical Engineering, California Institute of Technology, Pasadena, CA 91125, USA
*To whom correspondence should be addressed;
E-mail: zhendongli2008@gmail.com, gkc1000@gmail.com

The electronic structure of the metal cofactors of nitrogenase is central to biological nitrogen fixation. However, the P-cluster and iron molybdenum cofactor, each containing eight metal ions, have long resisted detailed characterization of their low-lying electronic states. Through exhaustive many-electron wavefunction simulation, we report on the full low-energy landscape of the P-cluster in three biologically relevant oxidation states. We trace the origin of the low-lying spectrum to the underlying local atomic states and their global recoupling, and how the interplay between antiferromagnetism, delocalization, and spin frustration as the geometry changes upon oxidation gives rise to the structure of the electronic landscape. Our results support the narrative that many-electron wavefunction simulations stand to provide a resolution of the complicated cofactors in nitrogenase at the electronic level.

The Fe-S clusters of nitrogenase, namely, the [Fe_4S_4] Fe-cluster of the Fe-protein, and the [Fe_8S_7] P-cluster and [$MoFe_7S_9C$] FeMo-cofactor of the MoFe protein, are the active sites for electron transfer and reduction in biological nitrogen fixation (*1–5*). The P-cluster and FeMo-cofactor, in particular, stand as peaks in the complexity of enzymatic cofactors, with eight

spin-coupled, open-shell, transition metal ions. Resolving their atomic and electronic structure has stood as a major challenge for experimental and theoretical spectroscopies. In the last decades, careful application of experimental techniques, including X-ray crystallography and spectroscopy, Mössbauer spectroscopy, and electron paramagnetic resonance, amongst others, has led to precise atomic structures, first for the Fe-cluster, followed by the P-cluster, and most recently, the FeMo-cofactor (*6, 7*). Like others, we have been working towards a similar goal of determining the electronic structure of the three clusters at a detailed, many-electron, level. A few years ago, we reported an *ab initio* picture of the electronic states of the Fe-cluster that revealed a rich low-energy landscape (*8*), with a density and variety of states far greater than previously thought. Here, we will present a comprehensive description of the electronic landscape of the P-cluster in its resting P^N state, one-electron oxidized P^{1+} state, and two-electron oxidized P^{OX} state relevant to its role in nitrogen fixation. As in our earlier work on the Fe-cluster, the many-electron calculations we perform are tractable due to the use of the compact matrix product state (MPS) representation (*9*) of open-shell electronic states, computed via the *ab initio* density matrix renormalization group (DMRG) (*10, 11*). However, the extraordinary complexity of the P-cluster necessitates a more sophisticated theoretical strategy that relies on our recent work on spin projection (*12*), in particular, to reliably explore the large number of electronic basins in the low-energy space.

Background on the P cluster

The hypothesized function of the P-cluster is to mediate electron transfer from the Fe-cluster to the FeMo-cofactor where nitrogen reduction takes place. The relevant states are the resting state P^N, the one-electron oxidized state P^{1+}, and the two-electron oxidized state P^{OX} (*13, 14*). Originally, the P-cluster was thought to contain 4Fe clusters (*15, 16*), but a clear picture of the atomic arrangement emerged from X-ray structures (*17, 18*). Here, we refer to the P^N and P^{OX}

structures reported by Peters et al (*17*) that revealed the [Fe_8S_7] core and two cubanes sharing a sulfur bridge in the P^N cluster, and the large structural rearrangement in the P^{OX} state, driven by coordination of Ser-β188 and Cys-α88 to Fe4 and Fe2 (*17*); and the recent P^{1+} structure (*18*), which only contains the serine hydroxyl coordination, and hence is midway between the P^N and P^{OX} structures. For comparison, we will also investigate a synthetic [Fe_8S_7] model cluster ([$\{N(SiMe_3)_2\}\{SC(NMe_2)_2\}Fe_4S_3]_2(\mu_6$-S)$\{\mu$-$N(SiNMe_3)_2\}_2$) (*19*) with a similar geometry to the P^N cluster, but with the P^{OX} electron count. In Figure 1, we highlight the redox-dependent structural rearrangements across P^N, P^{1+}, and P^{OX} .

The atomic structure of the P-cluster is now fairly well understood, but information on its electronic structure, the topic of this work, is more fragmentary. We summarize some representative experimental and theoretical data. In the P^N ground-state, EPR and Mössbauer spectra are consistent with a diamagnetic (S=0) ground-state, with all ferrous irons (*20*). The P^{OX} ground-state was first assigned to be paramagnetic with non-integer total spin due to an incorrect nuclearity assumption (*15, 16*), however, subsequent studies support a ground state with S=3 or S=4 (*21*). The P^{1+} ground-state EPR spectrum has been associated with a mixed-spin system with S=1/2 and S=5/2 (*22*). The sites of oxidation in P^{1+} and P^{OX} have not been established experimentally, but recent MCD measurements argued that in P^{1+} , the unpaired electron is localized to a single cubane based on similar spectral features of P^{1+} and the $[Fe_4S_4]^+$ cubane (*23*). On the theoretical front, pioneering work by Mouesca et al. (*24*) tried to shed light on the spin-couplings in P^{OX} which cannot be directly accessed experimentally. They suggested that the ground-state most likely consists of a left cubane in an $S_L = 7/2$ state (cubane II in (*24*)), and a right cubane in an $S_R = 1/2$ state (cubane I), recoupling to an $S = 4$ state. However, this analysis used a simplified model where the ground state was assigned to a single spin-coupled configuration, and further assumed that P^{OX} was composed of two $[Fe_4S_4]^+$ cubanes, based on the low-resolution P-cluster structure available at the time (*25, 26*), now known to be far from

the P^{OX} structure (*17*).

Given the scarce information on the electronic states, a qualitative understanding remains lacking. What are the relevant states of the Fe species in the different states of the cluster? How do electronic degrees of freedom combine to yield the overall ground state? What are the low energy excited states which come into play under small (e.g. geometric) fluctuations? And what is the relationship between geometry and electronic structure in P-clusters under oxidation? These are the questions we aim to answer using exhaustive simulation and new theoretical techniques.

Theoretical strategy

We will simulate the electronic structure using *ab initio* many-electron quantum mechanics. We recall why this is necessary for even qualitatively correct results. The most common electronic structure method applied to transition metal complexes is (broken-symmetry) density functional theory (BS-DFT) (*27–29*), sometimes augmented with model (e.g. Heisenberg) Hamiltonian analysis. This has produced important insights, but encounters limitations in systems that combine many open-shells with mixed valence character, as in the P-cluster. In the BS-DFT single-particle picture, each Fe center is assigned to a fixed spin up ($\uparrow$) or down ($\downarrow$) configuration, e.g., the BS configurations for P^{N} in Figure 2a. However, if the cluster is in a low-spin state, the global electronic state will be a superposition of many different spin configurations, as required by the overall low spin symmetry. In this case, BS-DFT neglects the global coupling and provides an incomplete, and often qualitatively incorrect, picture. To address this, one can use BS-DFT to extract parameters for a model many-spin Hamiltonian, which can then be diagonalized to obtain a coupled many-spin wavefunction, a simplification of the many-electron wavefunction. However, as we showed in work on the $[Fe_4S_4]$ cluster (*8*), simple model Hamiltonians typically do not contain many of the low-lying excited states, leading to an underestimation of

the density of the spectrum by an order of magnitude or more. A complete picture is thus only obtained when superpositions of both spin and orbital degrees of freedom are fully considered; this is provided by an *ab initio* many-electron simulation.

To make such a simulation tractable, we solve the Schrödinger equation exactly only within the space of the most important orbitals, a complete active space (CAS), and represent the wavefunction as a matrix product state (MPS) (*9*), a class of wavefunctions generated by the density matrix renormalization group (DMRG) (*10, 11*). In iron-sulfur clusters, the natural active space comprises the Fe $3d$ and S $3p$ (necessary for double exchange (*30*)) valence orbitals, which suffices to capture the qualitative low energy landscape (*8*). But even restricted to the active space, the number of relevant electron configurations is enormous, and grows exponentially with the cluster nuclearity: counting only configurations derived from Fe $3d$ orbitals, assuming all irons as Fe(III) for simplicity, there are $\sim 10^5$ low-spin configurations for [Fe_2S_2], $\sim 10^{10}$ for [Fe_4S_4], and $\sim 10^{22}$ for [Fe_8S_7]. To tackle this, the MPS provides a compression of the wavefunction, controlled by single parameter D, the bond dimension. Simulating with an MPS with finite D, followed by extrapolating $D \to \infty$, then yields an estimate of the exact solution, e.g. to within chemical accuracy in the active space, as we demonstrated in earlier work on the oxygen-evolving center (*31*) and the Fe-cluster (*8*).

However, there are additional complications when simulating the P-cluster beyond simply representing the wavefunction. This is because there is such a variety of qualitatively different low-energy electronic states, that the non-linear optimization of the MPS by DMRG is easily trapped in local minima, preventing access to the full spectrum. The different basins for the electronic states must thus be properly sampled in the optimization, similar to when studying competing phases in correlated materials (*32*). Note that although it is difficult to move between the basins, the local minima are themselves typically very close in energy, and in some cases, small changes in the theoretical model or experimental conditions can change their absolute

ordering. Thus, it is not necessarily meaningful to determine the absolute state ordering; instead we desire to determine the set of relevant (landscape of) low-energy states.

To address this, we designed an approach combining the simple enumerability of BS-DFT solutions with the representational power of MPS, within a framework of spin-projection. The procedure is outlined in Figure 2. The idea is to explicitly enumerate the spin isomers (which occupy electronic basins which are hard to convert between, as this involves multiple simultaneous spin flips) as done in BS-DFT calculations (e.g. for the [Fe_8S_7] model cluster (*33*)). The DMRG calculations are started in these basins, then additional excited states, arising from fluctuations of orbital and charge degrees of freedom, can be recovered by increasing the MPS bond dimension (D), which more efficiently explores these excitations, as they involve fewer electrons. Unlike in BS-DFT, we start from spin-projected product states, $\mathcal{P}_S|\Phi\rangle$ ($\mathcal{P}_S$ projects onto spin S, and $|\Phi\rangle$ is the BS configuration, see Figure 2a). As we have recently shown, this spin-projected product state is a special instance (bond dimension D_{SP}=1 for $|\Phi\rangle$) of the variational class of spin-projected matrix product states (SP-MPS) (*12*), and by increasing D_{SP} we can systematically relax the guess into the basin of interest, as we earlier demonstrated for [Fe_2S_2] and [Fe_4S_4] complexes (*12*). Here, we increase the bond dimension first to D_{SP}=50 (see Figure 2a), then convert the SP-MPS to the more computationally efficient spin-adapted MPS (SA-MPS) form (*34*), subsequently increasing the spin-adapted bond dimension D_{SA} to 10^3-10^4 (Figure 2d) to obtain a converged extrapolated energy. The intermediate step of using a correlated SP-MPS to seed the SA-MPS is important to stabilize the initial spin alignment and to avoid a rapid conversion to an undesired local minimum in the later SA-MPS optimization. (This is because a correlated SP-MPS with D_{SP}=50 can only be represented by a SA-MPS with a D_{SA} that is much larger, usually by a factor of 2-10 depending on the state (Figure 2c, and SI)). This composite approach robustly distills low-lying spin isomers with the correct spin symmetry, that are the candidates for the global low-energy states of the cluster.

Using the above, we carried out calculations on models for the P^N, P^{1+}, P^{OX} clusters derived from the cofactor and its surrounding residues embedded in a dielectric with $\epsilon = 4.0$, as well as the synthetic complex (*19*) (Figure 1). All Fe $3d$ and S $3p$ orbitals of the [Fe_8S_7] core as well as the bonding orbitals with other ligands were included in the active spaces for the *ab initio* DMRG calculations. This yields a CAS with 108 electrons in 71 orbitals, denoted by CAS(108e,71o), for the synthetic cluster, CAS(114e,73o) for P^N, CAS(117e,75o) for P^{1+}, and CAS(120e,77o) for P^{OX}, respectively; the size of the underlying many-electron Hilbert spaces range from 10^{31} to 10^{33} (Table S1). The basins of initial (spin-projected) product states for each complex are summarized in Figure 2b. In total, we examined 20 basins for the synthetic cluster ($S = 0$), 35 for P^N ($S = 0$), 70 for P^{1+} ($S = 1/2$ and $S = 5/2$), and 152 for P^{OX} ($S = 3$ and $S = 4$). Error bars are given when these can be estimated from extrapolation in D (see SI).

An important target of our calculations is to understand how the energetic landscape arises. Consequently, we computed local observables such as the charge $N_A = \langle \hat{N}_A \rangle$ and local spin projection $S^z_A = \langle \hat{S}^z_A \rangle$, as well as Fe-Fe spin-spin correlation functions $\langle \vec{S}_A \cdot \vec{S}_B \rangle$ (see SI). From these, we deduced how the global state appears from recoupling of local orbital and spin degrees of freedom, and the relationships between the electronic states in P^N, P^{1+}, and P^{OX} .

Results

The P^N cluster and its synthetic model

We begin with the simpler low-energy states of P^N and its synthetic model (Figure 3). We find the singlet (S=0) to lie below the triplet (S=1) and in agreement with Mössbauer and EPR spectra, the singlet ground state is an all-ferrous state. However, with the information from the many-electron wavefunction, we can understand how the individual Fe spins couple into the singlet state. From the spin-spin correlation functions, we deduce that it is composed of two AFM coupled [Fe_4S_4]^0 cubanes with effective spins S_{eff} ≈3.7, close to the classical idealized

antiferromagnetic spin coupling of S=-2+(2+2+2)=4 between the terminal and other three Fe(II) ions in the cubane. The cubanes in the P^N cluster appear to resemble the all ferrous $[Fe_4S_4]^0$ cluster in the super-reduced iron protein (*35*), which also has a paramagnetic S=4 ground state (*36*). (Indeed, the $[Fe_4S_4]^0$ ($S = 4$) cluster appears as an intermediate when assembling the P-cluster from a pair of neighboring $[Fe_4S_4]$ clusters in a nonenzymatic synthesis (*37*)).

The synthetic model also has a S=0 ground-state with the nominal oxidation states 6Fe(II)2Fe(III). However, even though the Fe oxidations of P^N and its synthetic model are different, we find that the ground states share similar AFM couplings (seen in the spin-spin correlation densities $\sigma_{\rm A}(\vec{r}) = \langle \vec{S}_A \cdot \sum_B \vec{S}_B(\vec{r}) \rangle$ with A=Fe1 in Figures 3a and 3b). This confirms earlier deductions from EPR and Mössbauer spectroscopies (*19*), as well as from a model Hamiltonian analysis (*33*). Similarly to the P^N cluster, the singlet arises from two AFM coupled cubanes, in this case $[Fe_4S_4]^+$ clusters with effective spins $S_{\rm eff} \approx 3.6$, close to the idealized coupling for one Fe(III) with three Fe(II) with S=-5/2+(2+2+2)=7/2. While the more common $[Fe_4S_4]^+$ ground-state has S=1/2 and a delocalized charge from resonance delocalization, the S=7/2 cubane state can arise if there is a competing external localizing force (*38*). In this case, the similarity between the P^N cluster and synthetic model spin coupling suggests that the external force for charge localization is the compact $[Fe_8S_7]$ core geometry, where the energetic lowering of the singlet ground state arises from maximizing the total number of AFM pairs between the cubanes.

We now turn to the low-lying excited states. Because there are so many ways to create excitations, we expect a dense electronic spectrum, even more complicated than the $[Fe_2S_2]$ and $[Fe_4S_4]$ spectra we discussed in Ref. (*8*). Nonetheless, we can group the low-energy excitations into classes (Figure 3c): (A) spin isomers, which retain the total spin (S=0) but differ by local reorientations of the spins and their couplings; (B) orbital excitations, where the electron configurations of the ions change; and (C) global spin excitations, where the cluster recouples into

a higher spin state (e.g. $S = 1$). Note that it is possible to have states which combine types of excitations, for example, a state in both classes A and B would recouple spins as well as change the electron configuration. Excitations in classes A and C are true many-electron excitations and cannot be fully described within BS-DFT, while excitations in class B are missed in typical model Hamiltonians, which do not contain all orbital degrees of freedom.

As shown in Figure 3, the lowest $S = 0$ excited states (B1-B4) of P^N correspond to orbital excitations (class B) with a different configuration of the Fe(II) $3d$ electrons (seen in the density difference $\Delta\rho(\vec{r})$), but with the same spin coupling scheme as the ground-state (see Figure S14). In particular, the lowest P^N excited state B1 arises from local $d \rightarrow d$ excitations in Fe8(II) at a very low energy of about 2kcal/mol (ca. 700cm^{-1}), much lower than the typical crystal field splitting (ca. 6000cm^{-1}) for the $e \rightarrow t_2$ transition in a perfect Fe(II)S_4 tetrahedral structure (*39*). This is because the local distortion of the right cubane lowers the crystal field symmetry, giving a transition between different components of the symmetry split e and t_2 orbitals. Other low energy excited states in class B correspond to linear combinations of local $d \rightarrow d$ transitions across different Fe atoms, resembling Mott excitons in metal-inorganic materials. Similar class B excited states can be seen in the synthetic cluster (Figure 3b) (although the low-lying Fe8(II) excitation is absent due to the different oxidation state of Fe8).

Excitations in classes A and C also appear at low energy. The lowest global spin excitation C1 is the simplest to understand and corresponds to the next rung in the Heisenberg ladder recoupling of the S=4 (P^N) or S=7/2 (synthetic model) cubane spins into an overall S=1 state, at an energy of approximately 0.6$\pm$0.3kcal/mol (P^N) (1.1$\pm$0.2kcal/mol (model)). The spin isomers are more complicated. As shown in Figure 3a, we find the next lowest P^N spin isomer at roughly 6.2$\pm$0.2kcal/mol above the ground state, corresponding to a rearrangement of the spin coupling in the right cubane (II) that swaps the ground-state spin configuration of Fe8 for that of Fe5. The total spin of the right cubane is left unchanged (see Figure S13), as is

its overall recoupling with the left cubane (I) into a singlet state. In contrast, the lowest spin isomer in the synthetic cluster (Figure 3b) corresponds to a higher total spin state ($S_{\text{eff}} \approx 4.3$) inside each cubane (the first excited state in the Heisenberg spin ladder for each cubane, i.e. S=-5/2+(2+2+2)+1=9/2) with the two spin excited cubanes recoupling back to a singlet. The analogous spin isomer to that in P^N can also be found in the synthetic cluster (state no. 17 in Figure S3b), but at much higher energy (ca. 20.2kcal/mol). This difference may be attributed to the Fe(III) oxidation states of Fe1 and Fe8, which breaks the cubane degeneracy, disfavoring the rearrangement of spins.

The oxidized P-clusters: P^{1+} and P^{OX}

We next move to the electronic structure of the oxidized P^{1+} and P^{OX} clusters. Due to the multiple Fe oxidation states, the recoupling of spins into a non-singlet ground state, and the opening of the structure which decreases the coupling between the cubanes leading to greater degeneracy, the low-energy spectrum is much more complex than that of P^N, especially for P^{OX}. We summarize the low-lying electronic states we find for P^{1+} ($S = 1/2$ and $S = 5/2$) and P^{OX} ($S = 3$ and $S = 4$) in Figure 4. Figure 5 shows how the spin-couplings of the relevant low-lying electronic states of the P-clusters evolve under oxidation from P^N, P^{1+}, to P^{OX}.

In P^{1+}, local charge analysis (see SI) suggests that oxidation occurs mostly on Fe4, which has the largest amount of Fe(III) character. Overall, however, the irons in the right cubane are more reduced than in P^N from the compression of the right cubane in P^{1+} and closer proximity of the ligands. The spin structure of the P^{1+} cluster is complicated. As mentioned above, the MCD spectra has previously been observed to resemble that of $[Fe_4S_4]^+$, from which it has been argued that the spin density is localized to a single cubane (*23*). However, the total spin arises from the coupling of cubanes each in non-singlet states, and consistent with that we find that the spin density $\rho_S(\vec{r})$ is delocalized over the whole cluster (Figures 4a and 4b). Instead, the

similarity between the P^{1+} and $[Fe_4S_4]^+$ spectra can be explained by the presence of localized (class B) excited states, rather than a localized spin density. Such low-lying orbital excitations within each cubane, similar to those in P^N, can clearly be seen (Figures S21 and S26).

Some of the spin-isomers in the low-lying P^{1+} states are evolutions of those in the P^N spectrum, while others represent new types of spin isomers. For example, the second S=1/2 state of P^{1+} (A2 in Figure 4a) has a spin-coupling resembling that of the P^N ground state, where the left cubane with effective spin $S_L = 4.1$ and the right cubane with $S_R = 3.8$ antiferromagnetically couple into a global $S = 1/2$ state (Figure 5). However, this state appears slightly above (0.7kcal/mol) a new type of S=1/2 spin isomer A1, where the left cubane has a different spin coupling pattern. In this lower state, two ferromagnetically coupled pairs with respectively $S_{\text{eff}} = 3.7$ (Fe1 and Fe4) and $S_{\text{eff}} = 3.6$ (Fe2 and Fe3), couple into a left cubane state with $S_L = 4.1$. The lowest S=5/2 state that we observe in the P^{1+} cluster lies below the lowest S=1/2 state by -2.7$\pm$2.8kcal/mol ($D = \infty$). In this state, the left cubane contains the same iron pairs as in the lowest S=1/2 state, but they are now recoupled antiferromagnetically into $S_L = 0.9$, while the spin coupling in the right cubane is more complicated and not easily interpreted, with an overall $S_R = 2.3$ (Figure 5).

The greater density of the electronic spectrum of the P^{OX} cluster is reflected in the experimental uncertainty about basic properties of even the P^{OX} ground-state, including its overall spin (*21*). We find that several states lie within the error bars of the calculations, and consequently, we will discuss the low-energy spectrum (Figures 4c and 4d) for $S = 3$ and $S = 4$ as a whole, rather than the ground- and excited-states separately. Our local charge analysis suggests that Fe2 and Fe4 are the main sites of oxidation consistent with the stabilization from the change in ligation, although all Fe's in the left cubane contain some ferric character, relative to the P^N cluster. The higher density of low-energy states associated with the opening of the $[Fe_8S_7]$ core structure after oxidation and weaker electronic coupling between the cubanes (as

compared with the strong AFM coupling in the ground state of P^N) can be seen in the smaller values of $\langle \vec{S}_A \cdot \vec{S}_B \rangle$ between irons on different cubanes (Figure 5).

The manifold of low-energy spin-isomers in P^{OX} can be rationalized in terms of recouplings of a small number of spin-coupled motifs in the left and right cubanes, indicated by the black lines in Figure 5. Many of these appear also in P^N and P^{1+}. For example, state A3 in the S=3 sector, is a recoupling of the left cubane with $S_L = 0.8$ from state A1 in the S=4 sector (or state A1 of P^{1+} with S=5/2), and the right cubane with $S_R = 2.7$ from state A2 in the S=4 sector. More generally, the relevant spin motifs in the left cubane form an approximate spin ladder ($S_L \approx 0.8, 1.5, 2.4, 3.3, 4.2$) arising from two coupled iron pairs (2Fe(1,4)-2Fe(2,3)), with the fractional S_L indicating strong fluctuations of local charges and spins associated with charge delocalization. The spin couplings of the right cubanes can be approximately viewed as arising from either 2Fe-2Fe or 3Fe-1Fe coupled spin systems. However, unlike in the P^N cluster, there is no simple classical picture of the spin-coupling in P^{OX}; each state results from a linear combination of multiple spin coupling schemes.

Determining the precise order of states in P^{OX} is very challenging and not fully resolvable at the current level of accuracy. For example, state A1 with $S = 3$ lies above state A1 with $S = 4$ by 1.4±0.8kcal/mol (when extrapolated in the DMRG calculations to $D = \infty$), while state A2 with $S = 4$ is higher than state A1 by 1.9kcal/mol at $D = 4000$, but becomes almost degenerate (0.0±0.8kcal/mol) with state A1 when extrapolated to $D = \infty$ (see SI). In addition to the above states, there is a low-lying $d \rightarrow d$ excitation on Fe8(II) from state A2 with S=4, at about 1.3kcal/mol above it (Figure S39). The very small energy differences mean that the states will be simultaneously populated at room temperature, and their ordering will change under small geometric fluctuations, for example, induced by changes in the protein environment.

We can attempt to correlate our computed low energy spectrum with the experimentally reported hyperfine parameters, using the phenomenological model developed by Noodleman

Table 1: Comparison of the experimental hyperfine parameters (internal magnetic fields $H_{\rm int}$ in kG, quadruple splittings ΔE_Q in mm/s, isomer shifts δ in mm/s) from Ref. (*16*) with the computed local charges $N_{\rm Fe}$ and spin projections $S^z_{\rm Fe}$ for the lowest $S = 3$ and $S = 4$ states of the P^{OX} cluster of *Azotobacter vinelandii*. The values of $N_{\rm Fe}$ for ground states of P^N and the synthetic model are listed as references.

Expt. (*16*)					P^{OX} ($S = 3$)		P^{OX} ($S = 4$)		$N_{\rm Fe}$	
no.	$H_{\rm int}$	ΔE_Q	δ	atom[a]	$N_{\rm Fe}$	$S^z_{\rm Fe}$	$N_{\rm Fe}$	$S^z_{\rm Fe}$	P^N	Syn
1	-287	-1.40	0.56	Fe1	6.24	0.52	6.24	-0.52	6.33	6.15
2	-237	+1.53	0.64	Fe2	6.15	0.47	6.15	0.44	6.46	6.32
3	-245	+0.57	0.40	Fe3	6.22	0.55	6.23	0.43	6.38	6.30
4	-151	+0.60	0.25	Fe4	6.07	1.04	6.08	-0.58	6.35	6.44
5	-259	+1.26	0.48	Fe5	6.34	-1.24	6.32	1.64	6.51	6.30
6	-237	-0.72	0.49	Fe6	6.41	1.42	6.40	1.66	6.48	6.32
7	201	+3.20	0.65	Fe7	6.33	1.55	6.28	1.74	6.33	6.45
8	223	+2.30	0.68	Fe8	6.18	-1.40	6.26	-1.33	6.32	6.15

[a] The index does not correspond to the no. in the first column.

et al. for iron-sulfur clusters (*24, 40*). Note that the experimental parameters themselves are obtained through fitting and are subject to considerable uncertainty, but we can compare the relative signs and magnitudes of the internal magnetic field $H_{\rm int}$ with local $S^z_{\rm Fe}$ for qualitative insight. As shown in Table 1, the hyperfine parameters have a 6:2 sign pattern similar to the lowest $S = 3$ state, whereas the lowest $S = 4$ state has a 5:3 sign pattern. Unfortunately, we cannot judge the appropriateness of the 5:3 pattern because it was excluded from the earlier experimental fit, as it was assumed then that the P-cluster only contained 4 irons. Out of the two 6:2 patterns, the small $S^z_{\rm Fe} = 0.47$ for Fe2, which is ligated with the amide-N, correlates with the small hyperfine parameter no. 4, while the increased charge on Fe2, which thus has more ferric character compared to the other sites, is consistent with the isomer shift of $\delta = 0.25$mm/s for the same iron (no. 4). Unfortunately, the reliability of fitted component no. 4 has also been called into question in the experimental study. Nonetheless, these caveats aside, the lowest $S = 3$ state appears to be the best candidate to match the experimentally derived hyperfine parameters.

Controllable states hypothesis

Given the extraordinary complexity of the low-lying electronic states in the P-cluster, one may wonder how this complexity is related to function. In general, a large state density is desirable in electron transfer, as one needs states at multiple energies to transfer electrons to and from different substrates. There are in principle two ways to obtain such a large number of states. The first is to create a (partially filled) band, as in a metallic solid catalyst, from the strong orbital overlap. The second is to have a large number of weakly coupled, localized orbitals at different energies, arising from different local environments. The latter is much closer to the situation in the P-cluster (and FeS clusters in general). We believe this second scenario, which gives rise to complex electronic structure from the many-electron recoupling of local states, is favoured in the nitrogenase clusters because of the greater controllability, as the local origin of the states means that changes in local geometry (or environment) can be used to control their energies. This is consistent with the intricate coupling between the low-energy landscape and the opening of the $[Fe_8S_7]$ core structure as one progresses from P^N to P^{1+} to P^{OX}.

Conclusions

In summary, we have shown that through many-electron wavefunction simulations, we can now unveil the detailed electronic structure of the P-cluster of nitrogenase. Our calculations report on a plethora of low-energy electronic states that shift in nature as the cluster moves between the P^N, P^{1+}, and P^{OX} states. Despite their apparent complexity, a careful analysis of many-electron correlation functions reveals how the local atomic configurations, spins, and spin-couplings combine to produce the global electronic states. The local antecedents of many of the states ties changes in electronic structure closely to the ligand environments of the individual ions, providing a biological route to the geometric control of electronic transfer despite the large

number of metal sites. Our work forms an element in the continuing story of the nitrogenase enzyme, where theory may now provide resolution of the structures at the electronic level, just as crystallography has advanced our understanding at the atomic level.

Author contributions

Z.L. and G.K.C. designed the study and wrote the manuscript. Z.L. performed the calculations. S.G. contributed to interfacing SP-MPS to SA-MPS used in the BLOCK code. Q.S. contributed to interfacing the PYSCF code with COSMO. All authors contributed to the discussion of the results.

References and Notes

1. H. Beinert, R. H. Holm, E. Münck, *Science* **277**, 653 (1997).

2. J. B. Howard, D. C. Rees, *Chemical reviews* **96**, 2965 (1996).

3. D. C. Rees, J. B. Howard, *Science* **300**, 929 (2003).

4. B. M. Hoffman, D. Lukoyanov, Z.-Y. Yang, D. R. Dean, L. C. Seefeldt, *Chemical reviews* **114**, 4041 (2014).

5. S. C. Lee, W. Lo, R. Holm, *Chemical reviews* **114**, 3579 (2014).

6. T. Spatzal, *et al.*, *Science* **334**, 940 (2011).

7. K. M. Lancaster, *et al.*, *Science* **334**, 974 (2011).

8. S. Sharma, K. Sivalingam, F. Neese, G. K.-L. Chan, *Nature Chem.* **6**, 927 (2014).

9. U. Schollwöck, *Ann. Phys.* **326**, 96 (2011).

10. S. R. White, R. L. Martin, *J. Chem. Phys.* **110**, 4127 (1999).

11. G. K.-L. Chan, S. Sharma, *Annu. Rev. Phys. Chem.* **62**, 465 (2011).

12. Z. Li, G. K.-L. Chan, *Journal of Chemical Theory and Computation* **13**, 2681 (2017).

13. J. M. Chan, J. Christiansen, D. R. Dean, L. C. Seefeldt, *Biochemistry* **38**, 5779 (1999).

14. K. Danyal, D. R. Dean, B. M. Hoffman, L. C. Seefeldt, *Biochemistry* **50**, 9255 (2011).

15. R. Zimmermann, *et al.*, *Biochimica et Biophysica Acta (BBA)-Protein Structure* **537**, 185 (1978).

16. B. Huynh, *et al.*, *Biochimica et Biophysica Acta (BBA)-Protein Structure* **623**, 124 (1980).

17. J. W. Peters, *et al.*, *Biochemistry* **36**, 1181 (1997).

18. S. M. Keable, *et al.*, *Journal of Biological Chemistry* **293**, 9629 (2018).

19. Y. Ohki, Y. Sunada, M. Honda, M. Katada, K. Tatsumi, *Journal of the American Chemical Society* **125**, 4052 (2003).

20. E. Münck, *et al.*, *Biochimica et Biophysica Acta (BBA)-Protein Structure* **400**, 32 (1975).

21. K. K. Surerus, *et al.*, *Journal of the American Chemical Society* **114**, 8579 (1992).

22. R. C. Tittsworth, B. J. Hales, *Journal of the American Chemical Society* **115**, 9763 (1993).

23. K. Rupnik, *et al.*, *Journal of the American Chemical Society* **134**, 13749 (2012).

24. J.-M. Mouesca, L. Noodleman, D. Case, *Inorganic Chemistry* **33**, 4819 (1994).

25. J. Kim, D. Rees, *Science* **257**, 1677 (1992).

26. M. K. Chan, J. Kim, D. Rees, *Science* **260**, 7 (1993).

27. L. Noodleman, J. G. Norman Jr, J. H. Osborne, A. Aizman, D. A. Case, *Journal of the American Chemical Society* **107**, 3418 (1985).

28. L. Noodleman, E. R. Davidson, *Chemical physics* **109**, 131 (1986).

29. K. Yamaguchi, T. Fueno, N. Ueyama, A. Nakamura, M. Ozaki, *Chemical physics letters* **164**, 210 (1989).

30. P. W. Anderson, H. Hasegawa, *Physical Review* **100**, 675 (1955).

31. Y. Kurashige, G. K.-L. Chan, T. Yanai, *Nature Chem.* **5**, 660 (2013).

32. B.-X. Zheng, *et al.*, *Science* **358**, 1155 (2017).

33. M. Shoji, *et al.*, *International journal of quantum chemistry* **106**, 3288 (2006).

34. S. Sharma, G. K.-L. Chan, *J. Chem. Phys.* **136**, 124121 (2012).

35. G. D. Watt, K. Reddy, *Journal of inorganic biochemistry* **53**, 281 (1994).

36. H. C. Angove, S. J. Yoo, B. K. Burgess, E. Münck, *Journal of the American Chemical Society* **119**, 8730 (1997).

37. K. Rupnik, *et al.*, *Biochemistry* **53**, 1108 (2014).

38. L. Noodleman, *Inorganic Chemistry* **30**, 246 (1991).

39. D. Coucouvanis, *et al.*, *Journal of the American Chemical Society* **103**, 3350 (1981).

40. J.-M. Mouesca, L. Noodleman, D. Case, B. Lamotte, *Inorganic Chemistry* **34**, 4347 (1995).

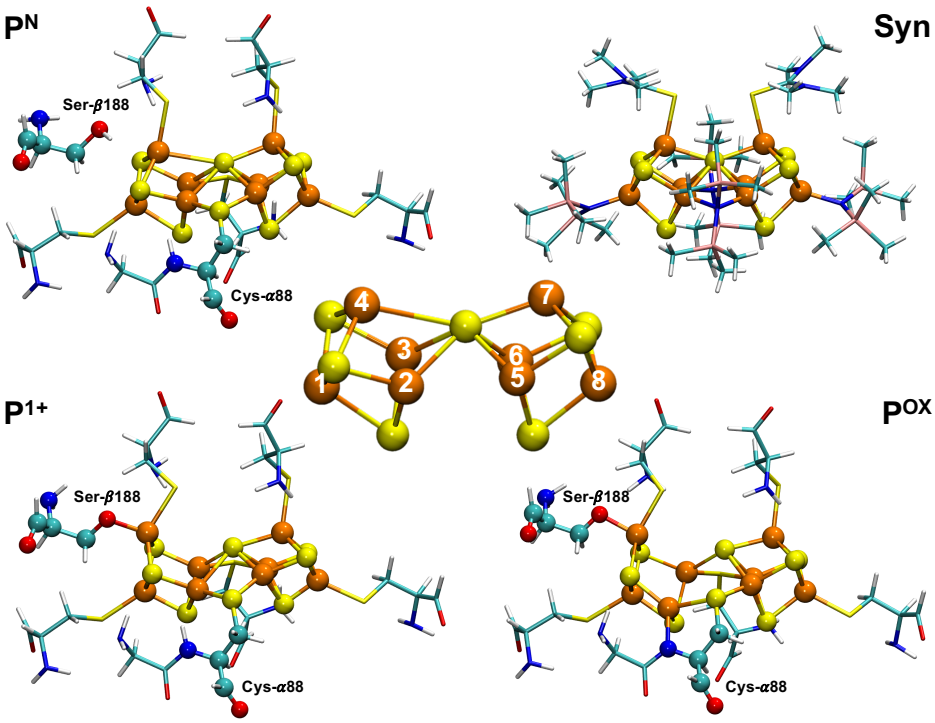

Figure 1: [Fe_8S_7] P-cluster models in the present study (PDB ID: 3MIN for P^N, 6CDK for P^{1+}, and 2MIN for P^{OX}, and the synthetic analog of the P^N cluster in Ref. (*19*)). The labels in the central figure number the indices of Fe atoms in the discussion. The redox-dependent structural rearrangement across P^N, P^{1+}, and P^{OX} involving Ser-β188 and Cys-α88 is highlighted. Color legend: Fe, orange; S, yellow; C, cyan; O, red; N, blue; H, white; Si, pink.

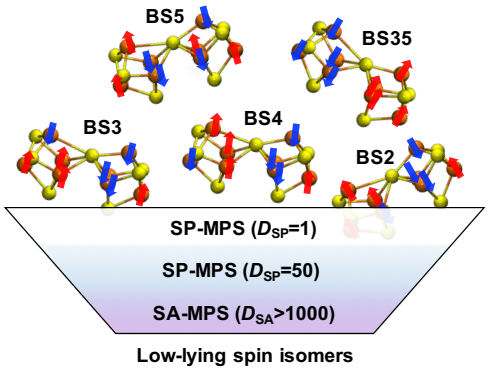

(a)

cluster	spin	class of initial guesses	no.
P^N	0	{4Fe^{2+}↑, 4Fe^{2+}↓}	35
Syn	0	{Fe^{3+}↑, Fe^{3+}↓, 3Fe^{2+}↑, 3Fe^{2+}↓}	20
P^{1+}	1/2	{Fe^{3+}↑, 3Fe^{2+}↑, 4Fe^{2+}↓}	35
	5/2	{Fe^{3+}↑, 3Fe^{2+}↑, 4Fe^{2+}↓}	35
P^{OX}	3	(a) {2Fe^{3+}↓, 5Fe^{2+}↑, Fe^{2+}↓}	6
		(b) {2Fe^{3+}↓, 4Fe^{2+}↑, 2Fe^{2+}↓}	15
		(c) {Fe^{3+}↑, Fe^{3+}↓, 3Fe^{2+}↑, 3Fe^{2+}↓}	40
	4	(a) {2Fe^{3+}↓, 5Fe^{2+}↑, Fe^{2+}↓}	6
		(b) {2Fe^{3+}↓, 4Fe^{2+}↑, 2Fe^{2+}↓}	15
		(c) {Fe^{3+}↑, Fe^{3+}↓, 3Fe^{2+}↑, 3Fe^{2+}↓}	40
		(d) {Fe^{3+}↑, Fe^{3+}↓, 4Fe^{2+}↑, 2Fe^{2+}↓}	30

(b)

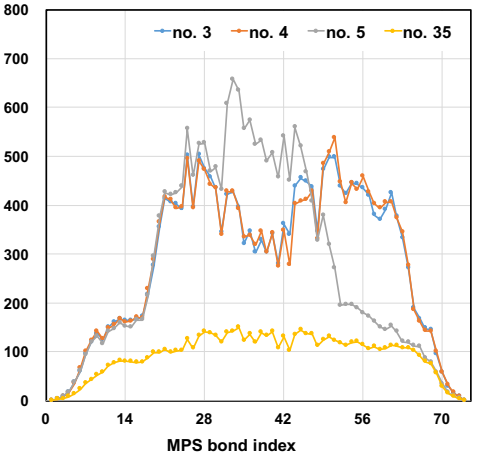

(c)

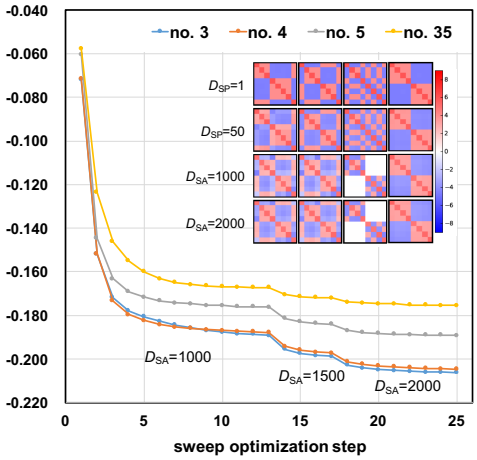

(d)

Figure 2: Methods for mapping out the low-lying electronic states. (a) Optimization procedure starting from different initial broken-symmetry (BS) product states, followed by spin-projection and SP-MPS optimization, and finally by SA-MPS with large bond dimensions. (b) Initial guesses obtained by distributing different iron states across the eight Fe atoms. (c) Distribution of bond dimensions $D_{\rm SA}$ of SA-MPS converted from SP-MPS with $D_{\rm SP} = 50$ for four different initial guesses, (d) Energy convergence ($E + 17492$ in Hartree) of SA-MPS versus optimization step with inset showing the convergence of the spin-spin correlation functions $\langle \vec{S}_A \cdot \vec{S}_B \rangle$ (red: positive, blue: negative) among the eight irons for the four states versus bond dimensions.

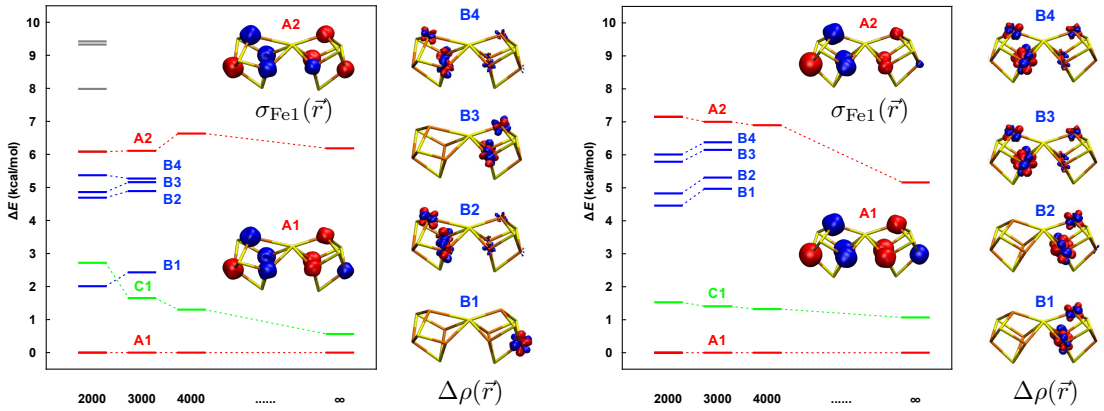

(a) $\mathrm{P^N}$ $(S=0)$ (b) Syn $(S=0)$

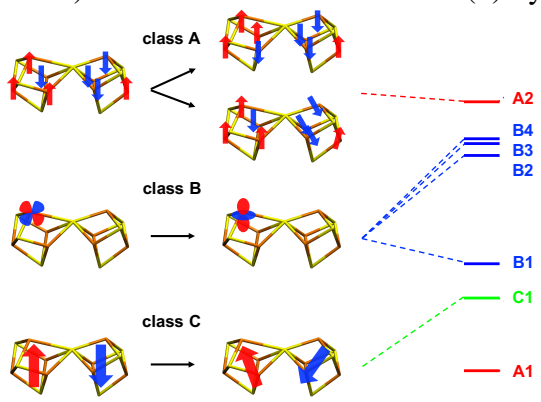

(c)

Figure 3: Results for (a) $\mathrm{P^N}$ and (b) synthetic cluster. Left panel: relative energies ΔE (kcal/mol) for spin isomers (black) computed from different initial guesses at $D = 2000$. The lowest two spin isomers (red) are further improved by progressively increasing D to 4000 and the total energies are extrapolated to $D = \infty$. Inset: spin-spin correlation density functions $\sigma_{\mathrm{A}}(\vec{r}) = \langle \vec{S}_A \cdot \sum_B \vec{S}_B(\vec{r}) \rangle$ with A=Fe1 for the first iron of these two spin isomers. Right panel: density differences $\Delta\rho(\vec{r})$ with respect to the ground state density for the lowest four excited states (blue) computed via a state-averaged DMRG calculation starting from the ground state at $D = 3000$. (c) Schematic of typical excitations. class A: spin isomers; class B: orbital excitations; class C: global spin excitations.

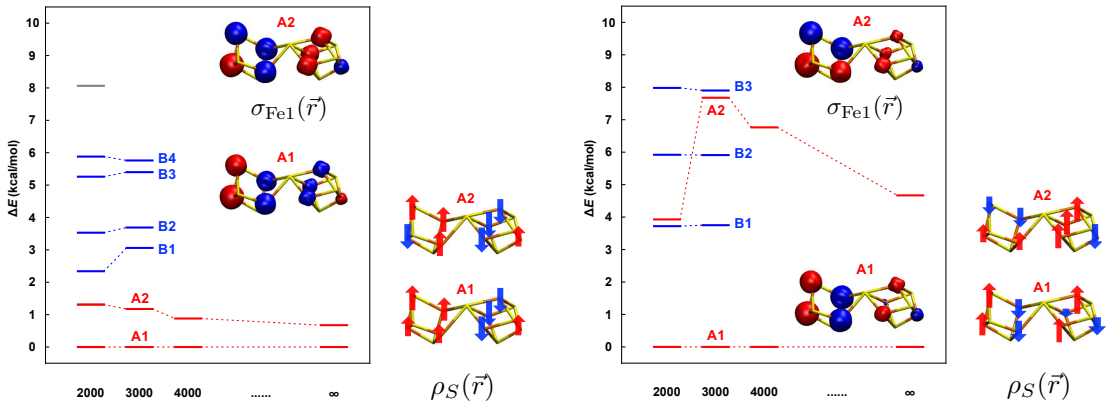

(a) P^{1+} ($S = 1/2$) (b) P^{1+} ($S = 5/2$)

(c) P^{OX} ($S = 3$) (d) P^{OX} ($S = 4$)

Figure 4: Results for the oxidized P-clusters: (a) P^{1+} with $S = 1/2$, (b) P^{1+} with $S = 5/2$, (c) P^{OX} with $S = 3$, (d) P^{OX} with $S = 4$. Left panel: see text in Figure 3. Right panel: schematic representation of the spin-density $\rho_S(\vec{r})$ of the lowest spin-isomers at $D = 3000$. The lowest $S = 5/2$ state of P^{1+} is lower than the lowest $S = 1/2$ state by -2.7±2.8kcal/mol computed with extrapolated energies, while the lowest $S = 4$ state of P^{OX} is lower than the lowest $S = 3$ state by -1.4±0.8kcal/mol computed with extrapolated energies.

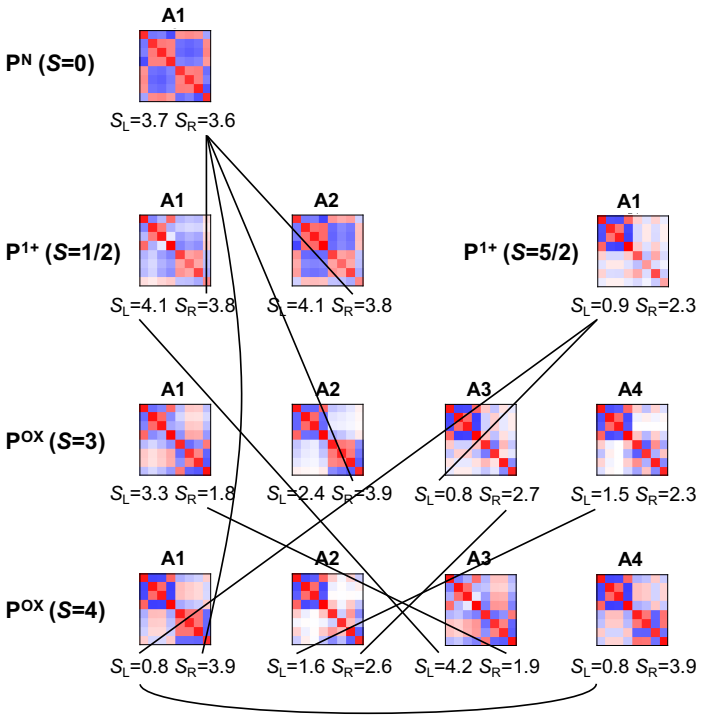

Figure 5: Relationships between spin-isomers in low-lying electronic states of the P-clusters. A black line between two states indicates that the same left or right cubane spin-coupling is shared by two states. Square graph: Spin-spin correlation functions $\langle \vec{S}_A \cdot \vec{S}_B \rangle$ among eight irons (red: positive, blue: negative). The effective spins of the left cubane S_L and the right cubane S_R are computed for the irons on the left and right cubanes, respectively.